N-doped porous transition metal-based carbon nanosheet networks as multifunctional electrocatalyst for rechargeable zinc-air batteries

Journal:	*ChemComm*
Manuscript ID	CC-COM-01-2019-000391.R1
Article Type:	Communication

Chem Comm

N-doped porous transition metal-based carbon nanosheet networks as multifunctional electrocatalyst for rechargeable zinc-air batteries

Jieting Ding,[a] Shan Ji,*[ab] Hui Wang,[a] Hengjun Gai,[a] Fusheng Liu,[a] Bruno G.Pollet,[c] and Rongfang Wang*[ad]

The development of cost-effective and highly efficient multi-functional oxygen reduction reaction and oxygen evolution reaction catalysts have attracted much research attention due to their great potential applications in many advanced clean energy storage and conversion technologies. Herein, highly efficient N-doped three-dimensional porous Co-Co$_3$O$_4$/C nanosheet network materials are developed as bifunctional electrocatalysts for rechargeable zinc-air batteries.

Currently, noble metal-based catalysts are required to catalyse the oxygen evolution reaction (OER) and oxygen reduction reaction (ORR) due to their fairly low overpotential.[1] Unfortunately, the scarcity and high price of the noble metal catalyst (e.g. Pt, Ru etc) impede widespread applications of catalysing the OER and ORR in metal-air batteries.[2-4] So far, many studies have focussed on low-cost and highly active transitional metal-based (such as Ni, Co, Fe, Mn and Mo) catalysts for OER/ORR in acid and alkaline media to reduce overpotentials.[5-8] However, these newly developed low-cost alternative materials still cannot compete with noble metal-based catalysts in terms of catalytic activity and stability. One of the main reasons why transitional metal-based catalysts´ properties cannot match those of noble metal-based catalysts is due to the aggregation of the particles of transition metal compounds, resulting in poor stability and activity caused by the loss of surface areas and active sites.[9]

It was reported that the electrochemical activity of these materials can be greatly improved if the transition metal nanoparticles are embedded into much stable materials, such as carbon and especially porous carbon ones.[10] Porous carbon materials with large surface areas can also efficiently facilitate the mass transfer and desorption/removal of hydrogen and oxygen on their surfaces during the electrochemical process,[11, 12] Combining transitional metal nanoparticles with carbon not only effectively avoid particle aggregation during electrochemical reaction, but also improve the catalytic activity due to the synergistic effect between the carbon and the transition metal.[13] In addition, the electrochemical properties of such combination can be tuned via changing the morphology and the porous structure of carbons.[14] The cobalt-based oxides, for instance Co$_3$O$_4$,[15, 16] MnCo$_2$O$_4$[17] have been deposited on N-doped carbon and graphene as catalysts for ORR. It was also found that integrating cobalt oxides into an interconnected nitrogen-doped carbon framework is an effective way to improve the electrocatalytic performance, as cobalt can improve the conductivity of the carbon matrix and enhance the charge transfer between the cobalt and carbon.[18] Although the cobalt-based carbon materials possess many advantages, the complicated synthetic procedure and costly precursors impede their use as catalysts for OER/ORR.

In this study, cobalt nanoparticles encapsulated in three-dimensional (3D) N-doped porous carbon network (Co-Co$_3$O$_4$/C) was developed as OER and ORR catalyst by a new method, in which NaCl salt was used as template to form the porous structure. This new synthesis method can yield mesoporous N-doped Co-based carbon without using any corrosive chemicals and complicated after-treatment procedures. The obtained Co-Co$_3$O$_4$/C catalytic materials were used as OER and ORR catalysts in alkaline media, which exhibited comparable electrochemical performances to noble metal-based catalysts for OER and ORR, in terms of electrochemical activity and stability.

Synthetic procedure of N-doped 3D porous Co-Co$_3$O$_4$/C nanosheet network is schematically represented in Fig. 1. The obtained mixtures were carbonized at high temperatures, during which NaCl melted and formed nanodroplets at 900 °C. These nanodroplets were immersed into the carbonized

[a.] State Key Laboratory Base for Eco-Chemical Engineering, College of Chemical Engineering, Qingdao University of Science and Technology, Qingdao, 266042, China, E-mail: rfwang@qust.edu.cn

[b.] College of Biological, Chemical Science and Chemical Engineering, Jiaxing University, Jiaxing, 314001, China, E-mail: jishan@mail.zjxu.edu.cn

[c.] Department of Energy and Process Engineering, Faculty of Engineering, Norwegian University of Science and Technology (NTNU), NO-7491 Trondheim, Norway

[d.] School of Chemistry and Chemical Engineering, Hunan University of Science and Technology, Xiangtan 411201, P. R. China

† Footnotes relating to the title and/or authors should appear here.
Electronic supplementary information (ESI) available: Experimental details, SEM, XRD, BET and the electrochemical performance of catalysts. See DOI: 10.1039/x0xx00000x

precursor during the carbonization and formed the porous structure in the final carbonized materials.[19] When there isn't NaCl in the precursors, only were solid blocks with irregular-shapes obtained (Fig. S1), which further confirm the key role of NaCl in the formation of porosity in the carbon. Since only NaCl was used as template to form the porous structure, it was fairly straight-forward to remove it without any complicated or costly post-processing steps.
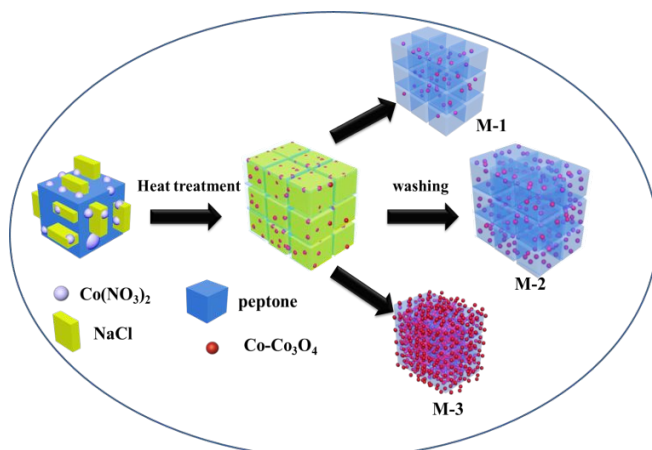

Fig.1 Synthesis route of Co-Co$_3$O$_4$/C samples.

The microstructure of the as-prepared carbonized samples was firstly investigated by scanning electron microscopy (SEM) and transmission electron microscopy (TEM). An open structured porous material with interconnected microporous network is observed in Fig. 2a,b. As shown in Fig. 2c,d, the thickness of the obtained sample were very thin, and irregular particles were encapsulated in the carbon network. It was observed that the size of the Co-Co$_3$O$_4$ nanoparticles was in the range of 10-25 nm. It is evident from the high resolution TEM images shown in Fig. 2e that the Co nanoparticles were embedded in the carbon material. The D-spacings of 0.157 and 0.204 nm, attributed to Co (511) and Co (111) planes, are clearly shown in the TEM image. Fig. 2e also shows that Co particles are wrapped around by carbon particles, and the D-spacing of 0.340 nm corresponding to C (002) plane is clearly found to surround the Co nanoparticles. The XRD patterns of M-2 are shown in Fig. 2f, in which there is a broad and weak peak at ca. 26° corresponding to C (002) plane, indicating the presence of small quantity of graphite. In addition to the graphite peak, the characteristic peaks of Co phase were found at 2θ of 43.94°, 51.4° and 75.82°. It can also be observed that there are three very weak diffraction peaks of Co$_3$O$_4$ at 2θ of 36.68°, 59.50° and 65.16°. The SEM and TEM images of M-1 and M-3 samples are shown in Fig. S2, highlighting very similar morphologies to the M-2 sample. However, particle aggregation was observed in the SEM and TEM images of M-3. As shown in Fig. S2c, only face-centered cubic (fcc) Co (0) phase was detected by XRD analysis, but the diffraction peaks of Co$_3$O$_4$ phase were found in the XRD pattern of M-3. For the M-1 sample, the amount of Co was small, which might indicate that Co particles were fully wrapped by the carbon particles. However, it is interesting to note that many Co particles were exposed to air to form Co$_3$O$_4$ in M-2 and M-3 samples. The SEM and TEM images of sample C are shown in Fig. S3. The morphology of C is similar to that of M-2, implying that the

presence of Co(NO$_3$)$_2$•6H$_2$O does not impact on the formation of the 3D porous carbon nanosheet network. The XRD pattern of C also shows a broad and weak peak at ca. 26° corresponding to the graphite (002) plane (Fig. S3d).
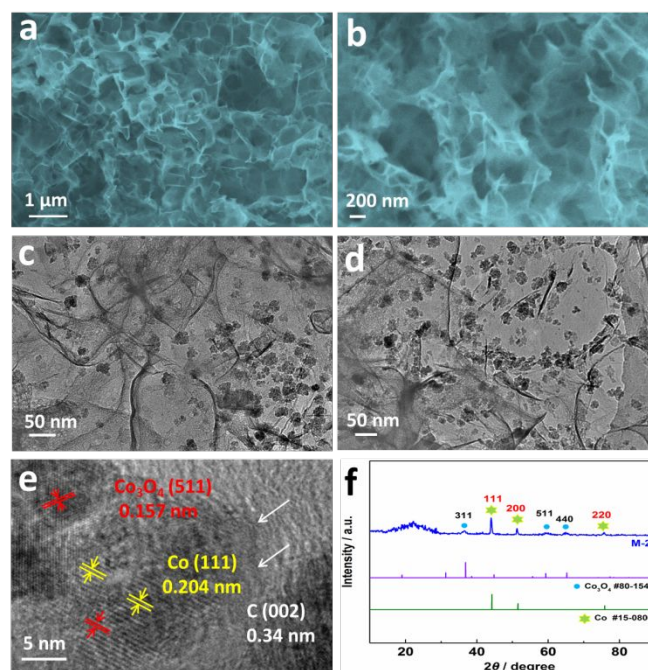

Fig.2 SEM images of M-2 (a, b), TEM and High-resolution TEM (HRTEM) images of M-2 (c-e); XRD pattern of M-2 (f).

Compositions and chemical states of the C and M-2 samples were investigated by X-ray photoelectron spectroscopy (XPS) analyses. As shown in Fig. 3a, the signals of N, O and C were observed in the C sample. Apart from the signals of N, O and C, Co was also detected in the M-2 sample. As shown in Fig. 3b, the fitted peaks of Co 2p spectrum at 786.5 eV are attributed to Co^{3+}, whereas the other two fitted peaks at 781.8 eV and 796.6 eV are indexed to Co^{2+}.[20] The peak at ca. 780.8 eV can be assigned to Co^0. The Co 2p XPS indicates that Co^0/Co^{3+}/Co^{2+} co-exist in the M-2 sample, which is in good agreement with the XRD results. Fig. 3c shows that the C 1s XPS spectrum of could be fitted into four peaks at 284.8 eV, 285.6 eV, 286.8 eV and 289.0 eV, corresponding to C–C, C-O/C–N, C=O and O=C–O bonds respectively, indicating that the sample had a graphitic structure.[21] The presence of C–O/C–N species further proves further that N atoms were successfully doped into the carbon network. Fig. 3d shows the high-resolution N 1s XPS spectra of M-2 and C, which can be deconvoluted into four peaks, namely the peaks at ca. 398.3 eV, 400.2 eV, 401.2 eV, 402.3 eV, 404.1 eV and 406.3 eV, corresponding to pyridinic N, pyrrolic N, graphite N, pyridinic N-oxide, π-π* and entrapped NOx respectively.[22] The content of these nitrogen species calculated from the XPS spectra of N 1s are shown in Fig. 3e, indicating that the amount of pyridinic N in the M-2 sample is much higher than in C. Although the role of each nitrogen species on the electrochemical performance is not well understood, it is generally accepted that pyridinic N is the active center for the electrocatalytic reaction.[23, 24] Fig. 3f shows the percentage of Co, O, N and C elements on the surface of M-2, calculated based upon the relative areas of the peaks of each element. It can be observed that the N content

doubled when $Co(NO_3)_2$ was introduced into the precursors. Introducing Co/Co_3O_4 into this N-doped carbon could result in more pyridinic N species formed in the final product, which is expected to produce more catalytic active sites. N_2 adsorption-desorption isotherms were employed to evaluate the porosity of M-1, M-2 and M-3 samples (Fig. S4). A narrow pore size distribution was observed for all three samples, there are two types of pores, i.e. micropore and mesopore. As shown in Fig. S3b, the external surface areas of M-1 and M-2 are much higher than that of M-3, indicating some of the porous structures can be blocked when there is a large quantity of Co/Co_3O_4 in the samples. Since the catalytic reaction only occurs on the surface, M-1 and M-2 are expected to exhibit better catalytic activity than M-3.
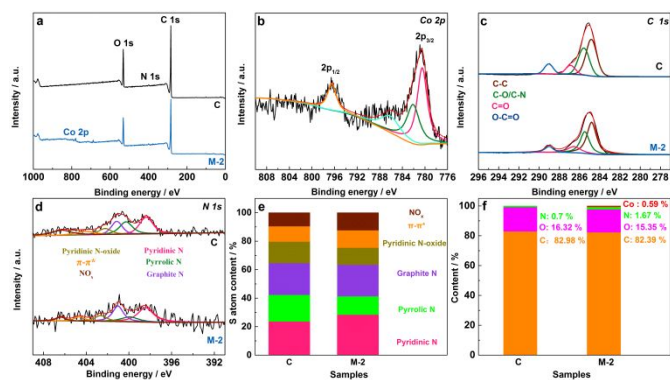

Fig. 3 XPS survey spectrum of C and M-2 (a); deconvoluted high resolution XPS spectra of Co 2p (b), C 1s (c) and N 1s (d); (e) contents of N species on C and M-2; element content of C and M-2 (f).

The OER activity of the as-prepare samples were investigated by linear sweep voltammetry (LSV) in 1 M KOH electrolyte at a scan rate of 5 mV s^{-1}. The LSV curves in Fig. S5a show that M-2 has the highest OER activity among all the tested catalysts, even more active than the state-of-the-art RuO_2 catalyst. The OER overpotentials for all samples are illustrated in Fig. S5b, demonstrating that M-2 has the lowest OER onset potential and lowest overpotential of +338 mV at a current density of 10 mA cm^{-2}, among all samples. Tafel plots were generated to study the OER electrocatalytic kinetics. As shown in Fig. S5c, the Tafel slope of RuO_2, C, M-1, M-2 and M-3 were found to be 59, 202, 60, 54 and 66 mV dec^{-1}, respectively. A lower Tafel slope represents higher OER activity. The Tafel results imply that M-2 has the most favourable OER kinetics among all samples. Continuous LSV cycling in 1 M KOH electrolyte was carried out to measure the OER durability for all catalysts. The LSV of the first (1st) and 3,000th cycle for M-2 and RuO_2 were plotted as shown in Fig. S5d and Fig. S6 respectively. It was found that the overpotential of M-2 shifted positively by +7 mV, which was lower than RuO_2 (+29 mV), indicating that M-2 has a better OER durability than RuO_2 in KOH medium. The OER overpotential for M-2 at a current density of 10 mA cm^{-2} was also compared with many representative catalysts reported in the literature and tabulated in Table S1.

As shown in Fig. S7a, the ORR for the M-2 sample exhibited a mixed process, i.e. a diffusion kinetics controlled step in the potential range of +0.9 to +1 V vs. RHE, and a diffusion controlled process when the potential was lower than ca. +0.9 V vs. RHE. Fig. S6b shows the linear Koutechy-Levich (K-L) curves at various potentials for the M-2 sample, suggesting

that the ORR on M-2 is a first-order reaction in the range +0.3 - +0.45 V vs. RHE. The electron transfer number for the ORR was also calculated based upon the slope of i^{-1} plotted vs. ω$^{-1/2}$. The inset of Fig. S7b shows that the ORR on the M-2 sample is a four-electron transfer process. The ORR LSV curve and K-L plots of Pt/C, C, M-1 and M-3 were also carried out and are shown in Fig. S8. The ORR on M-1 and C also went through a four-electron transfer process with relatively lower activities, suggesting that introducing Co species into the carbon matrix to achieve high ORR activities should be carefully carried out. Fig. S7c indicates that M-2 is the most active catalytic material toward the ORR among all the tested samples; it even outperforms Pt/C in terms of onset and half-wave potentials (Pt/C: +0.868 V vs. RHE and M-2: +0.891 V vs. RHE). The ORR performance of as-prepared and Pt/C samples were further evaluated by comparing their Tafel slopes as shown in Fig. S7d. It was found that the Tafel slope of M-2 was 67.87 mV dec^{-1}, smaller than that of Pt/C i.e. 95.5 mV dec^{-1}. The ORR durability of M-2 and Pt/C samples were determined by continuous linear sweep voltammetry (LSV) in KOH electrolyte. The first (1st) and 3,000th ORR LSV curves of M-2 and Pt/C are shown in Fig. S7e, S9 respectively. The figures show that the ORR half-wave potential for M-2 only increases by +10 mV after 3,000 cycles, but that of Pt/C increases by +34 mV; in other words, it was observed that the M-2 sample was more stable toward the ORR than Pt/C in KOH medium. In Fig. S7f, the ORR and OER were tested at the same conditions in 0.1M KOH solution to give an overall LSV curves for evaluating the performance. Usually, the overpotential ($\Delta E = E_{j=10} - E_{1/2}$) between the OER and ORR (OER potential at 10 mA cm^{-2} minus the ORR half-ware potential) is used to determine the overall oxygen electrocatalytic activity, i.e. a smaller ΔE value represents a better overall oxygen electrocatalytic activity. It is worthwhile noting that the M-2 sample exhibited a ΔE of +0.681 V vs. RHE, a value which was lower than that of the Pt/C + RuO_2 catalysts (ΔE = +0.738 V vs. RHE). The M-2 sample was also compared with representative catalysts reported in the literature (Table S2), clearly highlighting that the M-2 sample possesses outstanding catalytic activities. To have a better understanding of its catalytic activity, M-2 sample after acid treated was also tested for ORR and OER. The results were shown in Fig. S10, which indicated the catalytic performance of the sample after acid treatment decreased slightly after the acid treatment, which may be due to the dissolution of Co/Co_3O_4, namely Co/Co_3O_4 plays a critical role in the highly catalytic activity.
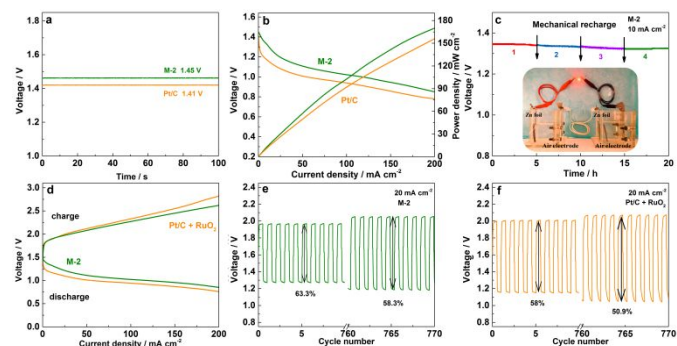

Fig. 4 Open circuit voltage of M-2 and Pt/C primary Zn-air batteries (a); Polarization and power density curves (b); (c) Long-time galvanostatic discharge of the primary Zn–air battery; Charging and discharging curves of M-2 and Pt/C+

RuO$_2$ cells (d); discharge and charge curves current density: 20 mA cm^{-2}, electrolyte: 6 M KOH +0.2M Zn(CH$_3$COO)$_2$ (e,f).

The M-2 sample was also evaluated in Zn-air battery cells. Initially, a primary Zn–air battery using M-2 as the electrocatalyst was assembled. As shown in Fig. 4a, the open cell voltage (OCV) of the primary cell containing M-2 was found to be +1.45 V as well as exhibiting good stability, better than the primary cell containing Pt/C. Fig. 4b shows the polarization and power density curves of the M-2 and Pt/C primary cells. The figure shows that at a current density of 200 mA cm^{-2}, the M-2 primary cell produces a power density of 171 mW cm^{-2}, slightly higher than the Pt/C primary cell (148 mW cm^{-2}). Usually, the primary cells can be charged by refilling the consumed Zn foil and electrolyte. After four times refilling, Fig. 4c shows that there is only slight drop in cell voltage, implying that the M-2 primary cell can be operated in KOH electrolyte with excellent durability. To further demonstrate the superior M-2 catalytic properties, two M-2 primary cells were connected in series to power a red LED light (2.0 V); it was observed that the LED operated for more than 12 h (Fig. 4c). Assembled M-2 rechargeable Zn-air cell was further investigated by galvanostatic charge-discharge and compared with Pt/C + RuO$_2$ cell as shown in Fig. 4d. The M-2 cell showed a higher potential response than Pt/C + RuO$_2$ cell in the testing current density region during the discharge, and a lower potential response for the M-2 cell was also observed during the charge. An "ideal" Zn-air battery should have high discharge and low charge cell voltages. The cell voltage profile of 770 charge and discharge cycles are shown in Fig. 4e and 4f. The voltaic efficiency was calculated based upon the discharge end cell voltage divided by charge end cell voltage. The initial round-trip overpotential was found to be +0.72 V with a voltaic efficiency of 63.3%. After 770 cycles, the round-trip overpotential increased to +0.85 V, and its voltaic efficiency decreased to 58.3%. For comparison purposes, the cycling stability of Pt/C +RuO$_2$ rechargeable cell was also tested under similar conditions. As shown in Fig. 4e and 4f, the M-2 cell exhibited a better cycling stability than Pt/C +RuO$_2$ cell in terms of overpotential and voltaic efficiency. The electrochemical results clearly demonstrate that the obtained M-2 not only possesses high intrinsic ORR and OER electrocatalytic activity and durability, but also delivers high cell performance and long cycling stability in real Zn-air batteries.

SEM and TEM analyses were carried out to investigate the samples' morphology change after stability testing experiments as shown in Fig. S11. Comparing the SEM and TEM images of M-2 after testing and images of fresh M-2 shown in Fig. 2 revealed no obvious changes in morphology of carbon, and no particle aggregation was found after stability experiments, further indicating that the M-2 has excellent stability toward ORR and OER in a KOH electrolyte.

In summary, the obtained N-doped 3D porous Co-Co$_3$O$_4$/C nanosheet networks are highly electrocatalytically active toward the ORR and OER. The Co-Co$_3$O$_4$/C networks can be successfully synthesized by using NaCl salt as template, which is much cost-effective and easier-to-remove than conventional organic templates used to prepare mesoporous materials. Compared to its carbon counterpart, XPS results of M-2 showed that more pyridinic N species formed on its surface after Co-Co$_3$O$_4$ nanoparticle could be introduced into the carbon matrix. The outstanding OER and ORR properties in KOH electrolyte can be mainly attributed to the synergistic effect between Co-Co$_3$O$_4$ nanoparticles and conductive N-doped carbon, which can efficiently improve the charge transfer between the electrode and electrolyte. Using NaCl as template to produce mesoporous carbon compounds can be a promising, scalable and industrial approach for producing catalysts with high electrocatalytic properties for metal-air batteries and water electrolyzers.

Conflicts of interest

There are no conflicts to declare.

Notes and references

1   Z. Guo, F. Wang, Y. Xia, J. Li, A. G. Tamirat, Y. Liu, L. Wang, Y. Wang and Y. Xia, *J. Mater. Chem. A*, 2018, **6**, 1443-1453.
2   J. Ding, P. Wang, S. Ji, H. Wang, V. Linkov, R. Wang, Electrochim. Acta, 2019, **296**, 653-661.
3   H. Peng, Z. Mo, S. Liao, H. Liang, L. Yang, F. Luo, H. Song, Y. Zhong, B. Zhang, Sci. Rep., 2013, 3, 1765.
4   J. Song, C. Zhu, S. Fu, Y. Song, D. Du and Y. Lin, *J. Mater.Chem. A*, 2016, **4**, 4864-4870.
5   X. Li, Z. Niu, J. Jiang and L. Ai, *J. Mater. Chem. A*, 2016, **4**, 3204-3209.
6   J. Ding, P. Kannan, P. Wang, S. Ji, H. Wang, Q. Liu, H. Gai, F. Liu, R. Wang, J. Power Sources, 2019, **413**, 209-215.
7   H. Wang, Z. Lu, S. Xu, D. Kong, J. J. Cha, G. Zheng, P. C. Hsu, K. Yan, D. Bradshaw and F. B. Prinz, *Proc. Natl. Acad. Sci. U. S. A.*, 2013, **110**, 19701-19706.
8   M. Shen, C. Ruan, Y. Chen, C. Jiang, K. Ai and L. Lu, *ACS. Appl. Mater. Interfaces*, 2015, **7**, 1207-1218.
9   J. Ding, S. Ji, H. Wang, J. Key, J.L.B. Dan, R. Wang, J. Power Sources, 2018, 374, 48-54.
10 M. Shun, W. Zhenhai, C. Suqin, G. Xiaoru, O. Kostya and C. Junhong, *Small*, 2015, **11**, 414-419.
11 Z. Wang, S. Xiao, Y. An, X. Long, X. Zheng, X. Lu, Y. Tong and S. Yang, *ACS. Appl. Mater. Interfaces*, 2016, **8**, 13348.
12 H. Li, F. Yue, C. Yang, P. Xue, N. Li, Y. Zhang and J. Wang, *Crystengcomm*, 2016, **19**, 64-71.
13 X. Cui, P. Ren, D. Deng, J. Deng and X. Bao, *Energy Environ. Sci.*, 2016, **9**, 123-129.
14 D. Jiao, R. Pengju, D. Dehui and B. Xinhe, *Angew. Chem. Int. Ed. Engl.*, 2015, **54**, 2100-2104.
15 M. Zhong, W. W. He, W. Shuang, Y. Y. Liu, T. L. Hu and X. H. Bu, *Inorg. chem.*, 2018, **57**, 4620-4628.
16 A. Aijaz, J. Masa, C. Rosler, W. Xia, P. Weide, A. J. Botz, R. A. Fischer, W. Schuhmann and M. Muhler, *Angew. Chem.*, 2016, **55**, 4087-4091.
17 K. Deng, C. Li, X. Qiu, J. Zhou, Z. Hou, *J. Electroanal. Chem.*, 2015, **755**, 197–202.
18 S. Guo, S. Zhang, L. Wu and S. Sun, *Angew. Chem.*, 2012, **51**, 11770-11773.
19 X. Shi, J. Key, S. Ji, V. Linkov, F. Liu, H. Wang, H. Gai, R. Wang, Small, 2018, 1802861.
20 K. Deng, X. Li, H. Huang, *Electrochim. Acta*, 2016, **204**, 84–91.
21 M. Zhong, W.-W. He, W. Shuang, Y.-Y. Liu, T.-L. Hu and X.-H. Bu, *Inorg. Chem.*, 2018, **57**, 4620-4628.
22 K. Deng, J. Zhou, H. Huang, Y. Ling, C. Li, Analytical Letters, 2016, 49, 2917–2930.
23 J. Ding, S. Ji, H. Wang, B. G. Pollet and R. Wang, *Electrochim. Acta*, 2017, **255**, 55-62.